Optics Communications 557 (2024) 130349

Contents lists available at ScienceDirect

Optics Communications

journal homepage: www.elsevier.com/locate/optcom

Experimental high sensitive local identification of azimuthal index of Laguerre–Gauss beams

Mirko Siano *, Bruno Paroli, Simone Cialdi, Stefano Olivares, Matteo G.A. Paris, Edoardo Suerra, Marco A.C. Potenza

Università degli Studi di Milano and INFN Sezione di Milano, Via G. Celoria, 16, Milan, 20133, Italy

ARTICLE INFO

Keywords:
Laguerre–Gauss beams
Optical vortices
Singular optics
OAM states
High sensitive detection
Birefringent crystals

ABSTRACT

In this work we experimentally demonstrate high sensitive strictly-local identification of azimuthal index of Laguerre–Gauss (LG) beams, with less than 160 photon counts. To this aim, detection of the azimuthal index of LG beams is performed with an innovative interferometer relying on a monolithic birefringent crystal, thus ensuring stability without the need of any feedback or thermal drift compensation. By first generating a reference interference pattern with a standard TEM_{00} mode, we then detect the value of the azimuthal index of a LG beam from the lateral shift of the pattern with respect to the reference one. An experimental setup has been realized to prove the effectiveness of the proposed scheme, which requires to access only a small portion (5%) of the entire wavefront. Moreover, being intrinsically endowed with extreme robustness and stability, we achieve effective high sensitive detection of the azimuthal index by collecting less than 160 photons only, while at the same time keeping the local features. Limitations and possible applications are also discussed.

1. Introduction

Radiation carrying Orbital Angular Momentum (OAM) [1] has gained a considerable attention in various scientific disciplines, effectively leading to the development of a novel branch of science and technology known as singular optics [2]. OAM radiation is a particular type of structured light endowed with unique intensity and phase properties. In particular, OAM beams exhibit twisting helical wavefronts with a phase singularity at the center, which corresponds to a donut-shaped intensity distribution with a minimum along the propagation axis. The helical wavefronts are characterized by an integer number l, known as the topological charge, which describes the number of 2π phase shift around the optical axis. Remarkably, the topological charge is also associated to the quantized orbital angular momentum $l\hbar$ of a single photon [3].

OAM beams have been exploited for different applications, e.g. to finely control and manipulate nanoparticles [4], to overcome the diffraction limit in imaging methods [5], in astronomical and astrophysical observations [6,7], to realize high-contrast and broadband coronagraphy [8–10], to investigate photoelectric rules and transition states not accessible with ordinary light [11,12]. In particular, the telecommunications sector has benefited the most from the additional degree of freedom offered by the topological charge [13–15]. By multiplexing different OAM states, high-capacity transmission systems over tens of Gbit/s have been recently realized [16–18] for both in-fiber networks [19,20] and free-space optical communications [21–24].

In all these disciplines and applications, detection of OAM states is of utmost importance for the full exploitation of OAM-based systems. To this aim, different interferometric [25–27], diffractive [28] and refractive [29,30] techniques have been proposed, leading to efficient sorters of OAM states [31,32] capable of fast (single-shot) performances [33]. Efficient detection and demultiplexing methods are provided by conjugate spiral phase plates and phase holograms [34], cascaded Mach–Zehnder interferometers [35], Dammann optical vortex gratings [36] and log-polar transformations [31]. More recently, new approaches to classify and demultiplex OAM beams have been introduced based on machine learning [37–39], with promising applications especially for OAM propagation through highly turbid media [40–43]. For a more complete discussion on generation and detection of OAM beams, the interested reader is referred to the following recent reviews [44–46].

Current state-of-the-art methods typically require collecting a substantial portion or the entire wavefront of the OAM beam, and in many cases the singularity should also be intercepted by the detector surface. Such requirements pose severe limitations in the detection of OAM states even in table-top laboratory setups, especially when the propagating beam becomes much larger than the detector size due to

* Corresponding author.
E-mail address: mirko.siano@unimi.it (M. Siano).

https://doi.org/10.1016/j.optcom.2024.130349
Received 16 October 2023; Received in revised form 17 January 2024; Accepted 28 January 2024
Available online 1 February 2024

the intrinsic photon beam divergence, in particular for higher values of the topological charge. More generally, high sensitive detection using only a small portion of the propagating beam is of particular interest and would represent a key-enabling technology paving the way for a more efficient class of non-destructive detectors and receivers. However, since a rigorous detection of OAM necessarily requires collecting the entire radiation wavefront [47–49], local detection techniques must rely on *a priori* knowledge and full control of the field structure of the incoming beam.

In this view, we have recently investigated and experimentally proven the possibility of introducing strictly-local detection methods based on Laguerre-Gauss (LG) beams, a class of OAM beams for which the value of the topological charge is related to the value l of the azimuthal index of the LG mode [50–53].

In this work, we experimentally demonstrate high sensitive, strictly-local identification of azimuthal index of LG beams by employing a monolithic interferometer based on a birefringent crystal. As such, the proposed scheme is intrinsically stable and does not require any feedback or thermal drift compensation. Remarkably, the method requires accessing a small portion of the wavefront only (also far from the LG beam axis), of the order of 5%, thus greatly improving over previous techniques. Moreover, being intrinsically endowed with extreme robustness and stability, it allows collecting sufficient statistics to identify the azimuthal index of very weak LG beams. We effectively achieve high sensitive identification of the azimuthal index of LG beams by collecting less than 160 photons only, while at the same time keeping the local features.

The paper is organized as follows. In Section 2 we briefly resume the principles of local detection of LG beams, and in Section 3 we describe the monolithic local interferometer based on a birefringent calcite crystal. In Section 4 we describe the experimental setup, and in Section 5 we illustrate experimental results, highlighting current limitations and discussing possible solutions. Perspectives on going in the large azimuthal index regime are highlighted in Section 6, while application of the method to weak LG beams with few photon counts is reported in Section 7. Finally, Section 8 closes the paper with some concluding remarks.

2. Local detection of LG beam states

Our method for local detection of LG beam states relies on the phase difference between different parts of the wavefront, which translates into a measurable shift of an interference fringe pattern, as detailed hereafter.

We consider a monochromatic LG beam with wavelength λ and azimuthal index l. By introducing cylindrical coordinates (r, θ, z), where r and θ refer to the radial and azimuthal positions on a plane transverse to the propagation direction z, the electric field $E(r, \theta, z)$ of the LG mode is described as follows:

$$E(r,\theta,z) = A(r,z)\exp[i\phi(r,\theta,z)]\,, \tag{1}$$

where $A(r,z)$ is the field amplitude

$$A(r,z) = E_0 \cdot \frac{w_0}{w(z)} \cdot \sqrt{\frac{2p!}{\pi(p+|l|)!}} \cdot \left(\frac{\sqrt{2}r}{w(z)}\right)^{|l|} \cdot \cdot L_p^{|l|}\left(\frac{2r^2}{w^2(z)}\right) \cdot \exp\left[-\frac{r^2}{w^2(z)}\right] \tag{2}$$

and $\phi(r,\theta,z)$ is the field phase:

$$\phi(r,\theta,z) = \frac{kr^2}{2R(z)} + \psi(z) + l\theta\,. \tag{3}$$

In Eqs. (2) and (3), E_0 is the overall field amplitude, w_0 is the beam waist, $w(z) = w_0\sqrt{1+(z/z_R)^2}$ is the $1/e$ radius of the Gaussian term, $z_R = \pi w_0^2/\lambda$ is the Rayleigh distance, $L_p^{|l|}$ is the associated Laguerre polynomial, $k = 2\pi/\lambda$, $R(z) = z[1+(z_R/z)^2]$ is the radius of curvature of the propagating wavefront, and $\psi(z) = (2p+|l|+1)\arctan(z/z_R)$ is the Gouy phase shift. The parameter p represents the number of radial nodes in the field amplitude, and $p+1$ is the number of rings in the intensity profile ($p = 0$ in this work).

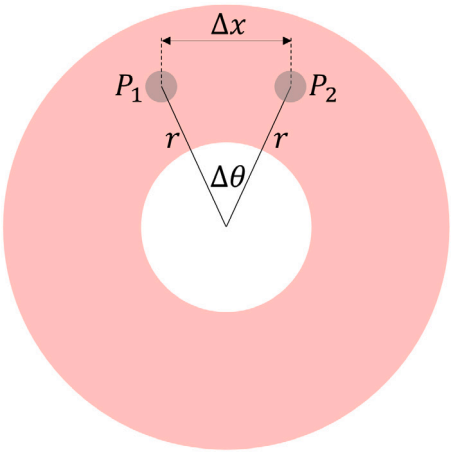

Fig. 1. Sketch of the local wavefront-division interferometer to identify the azimuthal index of LG beams. The two apertures at $P_1 = (r_1, \theta_1, z)$ and $P_2 = (r_2, \theta_2, z)$ (input ports of the interferometer) are located at the same radial distance $r_1 = r_2 = r$ from the beam axis and are separated by the amount Δx, i.e. by the angle $\Delta\theta \sim \Delta x/r$ with respect to the beam center.

We exploit the peculiar phase properties of LG beams, as described by Eq. (3), to achieve local identification of the azimuthal index l in a two-point detection scheme. To this aim, we employ a wavefront-division interferometer at a fixed distance z from the beam waist with the two apertures positioned at $P_1 = (r_1, \theta_1, z)$ and $P_2 = (r_2, \theta_2, z)$, respectively. The two apertures are located at the same radial distance $r_1 = r_2 = r$ from the beam axis and are separated by an amount Δx, thus subtend the angle $\Delta\theta = \theta_2 - \theta_1 \sim \Delta x/r$ with respect to the beam center, as shown in Fig. 1.

In this configuration, the phase difference $\Delta\phi = \phi(r_2, \theta_2, z) - \phi(r_1, \theta_1, z)$ of the electric field at the two apertures is given by the linear term $l\Delta\theta$ only, as it is apparent from Eq. (3). We recall that the position of the interference fringes in a wavefront-division interferometer depends on the phase difference of the electric field in correspondence of the two apertures [54]. For the $l = 0$ case, corresponding to a standard Gaussian beam illumination, $\Delta\phi = 0$ and the interference pattern is perfectly centered on-axis. Therefore, we can determine the value of the azimuthal index from the lateral shift δ of the fringe pattern with respect to the $l = 0$ case. Quantitatively, $\Delta\phi = 2\pi\delta\Delta x/(\lambda d)$, being d the distance of the observation plane from the two-point interferometer, and finally $l = \Delta\phi/\Delta\theta$.

Similarly, we can also directly detect changes of the azimuthal index from the relative position of the corresponding fringe patterns. In particular, given two values l_1 and l_2, the relative shift of the interference fringes is proportional to the change of the azimuthal index since $\Delta\phi_{l_2} - \Delta\phi_{l_1} = \Delta l\Delta\theta$, where $\Delta l = l_2 - l_1$.

Typically, apertures are used to select the points P_1 and P_2. These might be slits or pinholes in a typical Young's interferometer [50,51], or optical surfaces intercepting the incoming LG beam wavefront in more advanced schemes based on a combination of mirrors and beam splitters [52,53]. In the following section, we show how apertures are not required for the proposed interferometer relying on a birefringent crystal.

3. A strictly-local monolithic interferometer based on a birefringent crystal

We exploit the birefringent nature of a calcite crystal to realize a strictly-local monolithic wavefront-division interferometer endowed with extreme stability, robustness and resistance to external perturbations.

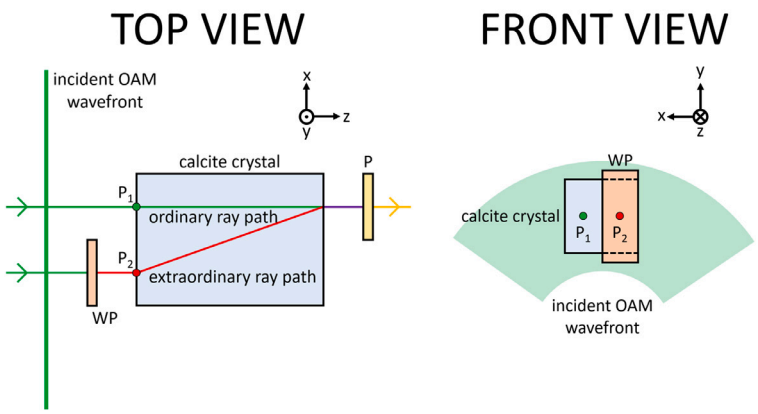

Fig. 2. Top view (left) and front view (right) of the monolithic interferometer scheme based on a birefringent calcite crystal. The case of a perfectly collimated incident beam is depicted, see text for details. In both views, the orientation of the x-y-z axes is also shown for completeness. WP: $\lambda/2$ wave plate; P: 45 degree polarizer. Color code: vertical polarization parallel to the polarization axis of the crystal in green, horizontal polarization in red, elliptical polarization in violet, 45 degree linear polarization in yellow.

A schematic diagram of the working principles of our monolithic interferometer is reported in Fig. 2. We consider two points P_1 and P_2 on the front face of the crystal. They are at the same radial distance r from the LG beam axis and are separated by Δx, i.e. they subtend the angle $\Delta\theta \sim \Delta x/r$ with respect to the beam center. We assume perpendicular incidence, with the polarization of the LG beam at P_1 parallel to the polarization axis of the ordinary ray of the crystal, while the polarization at P_2 is rotated along the orthogonal direction. In this configuration, for a suitable value of Δx, two parallel light rays incident on the crystal at P_1 and P_2 will perfectly superimpose at the exit of the crystal and can therefore interfere upon projection along a common polarization direction. The particular value of Δx for which this occurs is determined by the birefringent properties of the crystal, and it is therefore crystal-dependent. Notice that the same principle is at the basis of the splitting of a single beam into two beams with orthogonal polarizations by birefringent crystals, as typically reported in textbooks.

The proposed configuration can be realized in practice by aligning the polarization axis of the incoming LG beam at P_1 with the polarization axis of the ordinary ray of the crystal, and then by covering P_2 with a $\lambda/2$ wave plate oriented at 45 degrees. Thanks to this scheme, the electric fields at P_1 and P_2 now have orthogonal polarizations and propagate through the crystal along the ordinary and extraordinary paths, respectively. They then superimpose on an observation plane downstream the crystal. By projecting both fields along a common polarization direction with a linear polarizer, interference fringes form with intensity

$$I(x) = 4I_0 \frac{\cos(k_f x + l\Delta\theta + \phi_0) + 1}{2}, \tag{4}$$

where $I_0 = |A(r,z)|^2$ is the intensity of the incident beam, $k_f = 2\pi/\Lambda$, Λ is the spatial period of the interference fringes, and ϕ_0 is the phase shift due to the difference between the ordinary and extraordinary paths. In writing Eq. (4), we have assumed that fringes are oriented along the vertical direction y, being x the horizontal axis. Notice that the dependence on the azimuthal index of the LG mode in Eq. (4) is given only by the linear term $l\Delta\theta$, since k_f and ϕ_0 are independent on l.

For the case of a perfectly collimated incident beam, the two rays with orthogonal polarizations exit the crystal from the same point and propagate collinearly and perfectly overlapped along the same direction, giving rise to a uniform intensity distribution upon interference ($\Lambda \to \infty$ in Eq. (4)). These two rays originate from points P_1 and P_2 separated by a particular value of Δx which depends on the crystal and the radiation wavelength. It is 4.3 mm in our case.

Contrarily, if the incident wavefront is endowed with a finite curvature, the two rays emerge from the crystal from two different positions and superimpose on the observation plane with a finite angle Θ, thus forming interference fringes with finite periodicity $\Lambda \sim \lambda/\Theta$. In this case, the two rays originate from points P_1 and P_2 whose separation Δx is smaller compared to the case of a perfectly collimated beam, the exact value depending on the actual wavefront curvature. In our case, for a radius of curvature of 2.6 m, the actual separation between the two points P_1 and P_2 is 3.3 mm.

The question remains on how to locate the points P_1 and P_2 on the front face of the crystal. Here comes the beauty of the proposed scheme, since the interference is realized with any couple of light rays incident on the crystal front face with the proper separation Δx. Clearly, by varying the absolute position of P_1 and P_2 on the front face of the crystal, the corresponding rays will exit the crystal at different lateral positions. This generates two superimposing bundles of rays, i.e. wavefronts, endowed with orthogonal polarizations, that can therefore interfere upon projection onto the same polarization direction. Notice that, to this aim, it is only required that the incoming rays at all points P_1 and P_2 have orthogonal polarizations. Referring to our scheme, this also implies that the rays that can actually interfere are only those intercepting the crystal front face within a region centered in correspondence of the edge of the $\lambda/2$ wave plate and with horizontal width $2\Delta x$. Rays outside this region are not superimposed at the crystal exit, therefore cannot interfere. Since there are no limitations along the vertical direction other than the vertical extension of the crystal L, we can also conclude that only the area $2\Delta x L$ is utilized for the interference. In our case, this corresponds to a fraction $f = 2\Delta x L/(\pi r^2) = 5\%$ of the entire incident wavefront, with $L = 11$ mm and $r = 21$ mm.

4. Experimental setup

A proof-of-principle setup, sketched in Fig. 3, has been realized to prove the effectiveness of our local detection method. A He-Ne laser beam with $\lambda = 632.8$ nm is spatially filtered and collimated. The resulting Gaussian beam has a diameter of 3.7 mm ($1/e^2$ intensity value) and illuminates a Digital Micromirror Device (DMD). A computer-generated fork hologram is projected onto the DMD to convert the Gaussian beam into a LG beam. The first diffraction order is selected, corresponding to a LG beam with the desired azimuthal index. The LG beam is then properly aligned along the horizontal and vertical planes and sent to the interferometer by means of two mirrors. The beam is expanded through a positive lens before impinging onto a birefringent calcite crystal (Thorlabs BD40). The beam diameter at the entrance of the crystal is roughly 33 mm for $l = 0$, i.e. for a standard Gaussian beam ($1/e^2$ intensity value). Half of the birefringent crystal is covered by a $\lambda/2$ wave plate, oriented at 45 degrees with respect to the vertical polarization of the incoming LG beam. This ensures that the transmitted portion of the LG beam wavefront acquires a horizontal polarization. The vertically and horizontally polarized portions of the incoming LG beam propagate inside the calcite crystal along the directions parallel

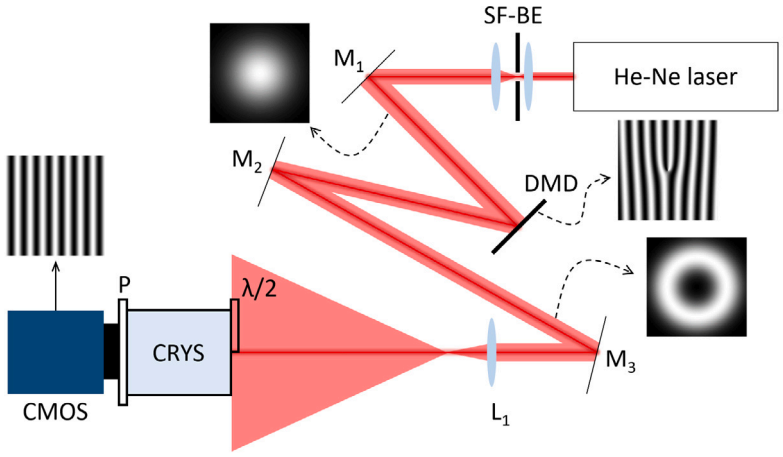

Fig. 3. Experimental setup. SF-BE: spatial filter and beam expander; M1, M2, M3: mirrors; DMD: Digital Micromirror Device; L1: positive lens; $\lambda/2$: half-wavelength wave plate; CRYS: birefringent calcite crystal; P: 45 degrees polarizer.

to the ordinary and extraordinary rays, respectively, and superimpose downstream the crystal. A 45 degrees polarizer ensures interference between these two wavefronts. Interference fringes are acquired with a standard CMOS camera (Thorlabs DCC1240M, 1280 × 1024 pixels, 5.3 × 5.3 μm^2 pixel size).

5. Results and discussion

The interference patterns acquired with the CMOS camera at the exit of the monolithic interferometer are shown in Fig. 4 (top) for $l = -1$ and $l = -4$. Notice the different intensity levels, resulting from the dependence of $A(r, z)$ on the azimuthal index l of the LG mode (see Eq. (2)). This effect does not influence the fringe position, which only depends on the phase properties of the incident LG beam, and can actually be compensated by a proper normalization, as detailed below.

The interference patterns in Fig. 4 (top) are numerically integrated along the vertical direction to extract the interference profiles shown in Fig. 4 (bottom), while at the same time reducing noise. Notice that the rightmost portion of the pattern is characterized by the expected interference fringes, while the leftmost portion shows distortions introduced by diffraction at the edge of the $\lambda/2$ wave plate.

To check the effectiveness of the interferometer, we precisely measure the phase shift of the fringes by changing the azimuthal index from $l = -1$ to $l = -4$. We report in Fig. 5 the same integrated intensity profiles as in Fig. 4 (bottom) in the range 5.6–6.6 mm, properly normalized according to

$$I_n(x) = \frac{I(x) - \min\{I(x)\}}{\max\{I(x) - \min\{I(x)\}\}}, \tag{5}$$

where $I(x)$ is the intensity profiles in Fig. 4 (bottom) and $I_n(x)$ is the corresponding normalized version. Normalization according to Eq. (5) allows to identify the different values of the azimuthal index from the position of the fringes despite the absolute intensity values of the $l = -1$ and $l = -4$ LG beams substantially changes, as previously mentioned. The measured lateral shift of the interference pattern when changing the azimuthal index from $l = -1$ to $l = -4$ corresponds to a phase shift of 0.513 ± 0.007 rad, in good agreement with the calculated value $\Delta\phi_{th} = \Delta l \Delta\theta = 0.47 \pm 0.05$ rad. The main source of uncertainty for the calculated value is the position of the local interferometer with respect to the LG beam axis ($r = 21 \pm 2$ mm). The experimental phase shift was evaluated using the phase parameters extracted by a least squares method to Eq. (4). The experimental uncertainty stems from the uncertainty on the fit parameters.

Some limitations of the proposed approach are listed in the following, alongside a discussion of possible solutions:

- the two points P_1 and P_2 should be at the same radial distance from the LG beam axis in order to neglect the contribution coming from the wavefront curvature in Eq. (3). This condition can be easily fulfilled in a laboratory setup, where the position and orientation of the interferometer can be finely tuned and controlled. Furthermore, it does not represent a strict limitation when the LG beam wavefront is much larger than the crystal, since in this case the radial phase variations due to the finite wavefront curvature are small on the typical length-scale of the detector;
- related to the previous point, air turbulence might induce scintillation and dynamic changes in the wavefront curvature and direction. As a consequence, the curvature component in the LG beam phase, as well as the actual position of the beam waist, might vary in an unpredictable way, and additional wavefront tilts can influence the interference patterns as well. For moderate turbulence, possible solutions are the use of an auxiliary beam in a composite scheme [51] or the realization of a phase-locked interferometer by means of piezo-actuators [52]. In general, however, turbulence in the atmosphere might severely affect and invalidate local detection of the azimuthal index of LG beams, and more in-depth investigations are required to quantify the effects of random phase distortions on local detection methods;
- more fundamentally, local detection is strictly valid for perfect eigenmodes such as Laguerre-Gauss and Bessel-Gauss modes. In real experiments the radiation beam might suffer phase distortions, resulting for example from surface imperfections of the optical components. Such phase inhomogeneities are typically localized, and can in principle degrade the performances of local detection methods. Accurate alignment of the setup and high-quality optical components ensure minimization of these effects. This is the case of the presented work, where phase distortions are kept to a minimum, as shown by the good agreement between experimental results and theoretical expectations. Moreover, if possible, one can take advantage of the localization of such phase defects and scan different positions of the interferometer until a good correspondence with the input LG beam state is found;
- in principle, different vertical positions on the observation screen correspond to slightly different angles $\Delta\theta$. Quantitatively, since the vertical extension of the crystal used in this paper is $L = 11$ mm, the corresponding maximum and minimum angles in our case are $\Delta\theta_{max} = \Delta x/(r - L/2) = 0.21$ rad and $\Delta\theta_{min} = \Delta x/(r + L/2) = 0.12$ rad, respectively. Here $r = 21$ mm is the distance of the center of the crystal front face from the LG beam axis, and $\Delta x = 3.3$ mm as previously detailed. The relative difference with respect to the nominal angle $\Delta\theta = \Delta x/r = 0.16$ rad is in the order of 27%. However, in practice, the integration along the vertical

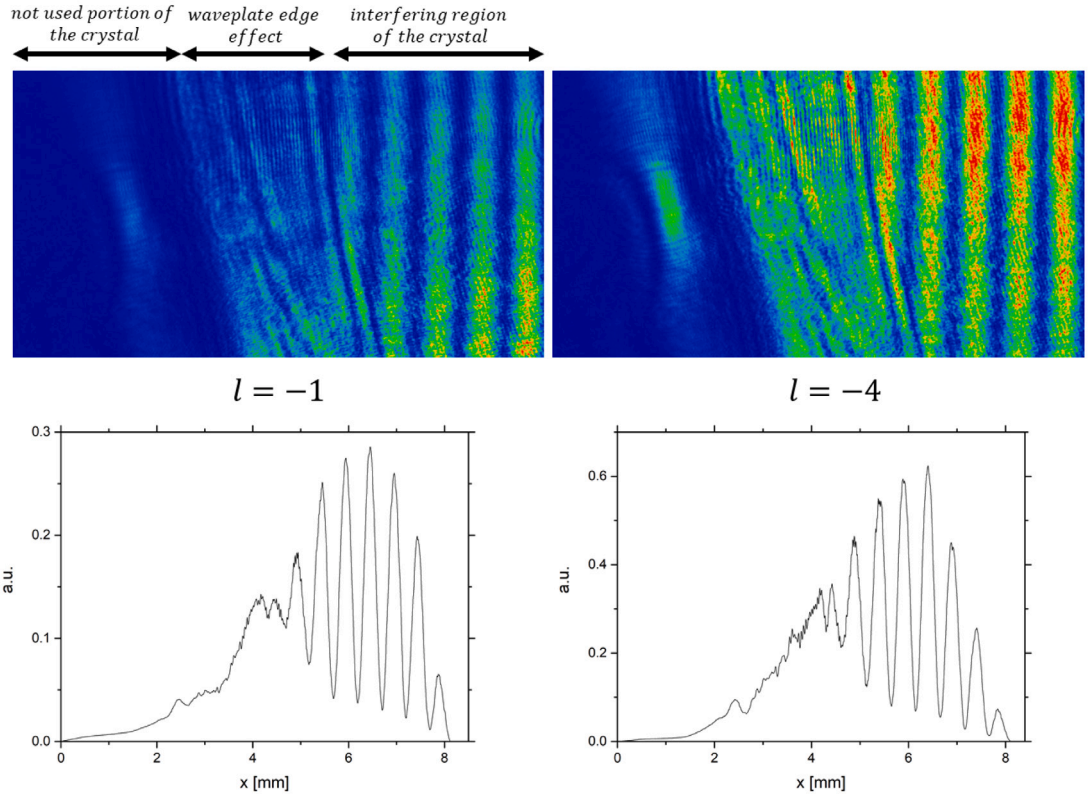

Fig. 4. (Top) Portion of the interference pattern generated by the monolithic interferometer for values of the azimuthal index $l = -1$ and $l = -4$. Interference fringes generated by the superposition of the beams propagating along the ordinary and extraordinary paths are clearly visible to the right (due to a small tilt between the camera and the crystal, images have been rotated to align the interference fringes along the vertical direction). (Bottom) Intensity profiles of the interference patterns integrated along the vertical direction.

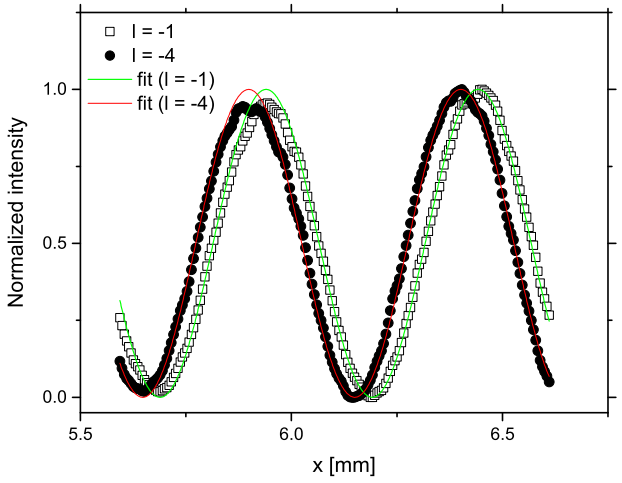

Fig. 5. Normalized intensity $I_n(x)$ of the integrated interference patterns generated with the monolithic interferometer for values of the azimuthal index $l = -1$, $l = -4$. The red and green curves represent fits to Eq. (4) to extract the phase parameters.

direction is performed only within the finite extension of the camera sensor (5.4 mm). In this case, the effective maximum and minimum angles are therefore 0.18 rad and 0.14 rad, respectively, with a relative deviation of 12% with respect to the nominal one. This value is comparable to the relative uncertainty (11%) of theoretical calculations due to the uncertainty in exactly locating the center of the LG beam during the experiment.

6. Perspectives and challenges for large azimuthal index values

The finite size of the crystal limits the range of possible azimuthal indices that can be detected. Since the radius of the annular intensity distribution of LG modes increases with the absolute value of the azimuthal index, one should ensure that the desired LG beam intercepts the interferometer while at the same time producing a detectable signal. In our case, with detection performed with the CMOS camera, this would limit us to $l < 13$, according to numerical estimations based on Eq. (2). Higher values of the azimuthal index would be detectable only by moving the crystal further away from the beam axis. For example, at the maximum radial distance at which the TEM_{00} still gives a detectable signal, the limit would be $l < 26$ in our case. For even larger values of the azimuthal index, the interferometer should necessarily be operated at two different radial positions: one in correspondence of the TEM_{00} mode to set the reference position of the interference fringes, and the other in correspondence of the LG beam to infer the azimuthal index from the lateral shift of the fringes. In this case, the change of the angle subtended by the interferometer at the two different radial positions should be carefully considered as well.

Another fundamental limitation arises from the finite periodicity of the interference fringes. For values of the azimuthal index high enough, the lateral shift of the interference pattern progressively increases and eventually exceeds the fringe periodicity, thus leading to a possible degeneracy with other LG beam states with lower l values. Therefore, only a finite number of different LG modes can be detected depending on the fringe periodicity and the detector pixel size, although advanced numerical algorithms achieve sub-pixel resolutions. Other possible solutions might rely either on simultaneous measurements of both the interference pattern and the overall intensity of the incident beam, or on fine tuning of the geometrical parameters of the interferometer

Table 1
Normalized and absolute counts obtained with the monolithic interferometer working in the regime of weak LG beams.

LG beam azimuthal index	Normalized counts	Absolute counts
$l = +2$	0.77	160
$l = +1$	0.54	157
$l = -1$	0.31	120
$l = -2$	0.22	57

(namely, the angle subtended with respect to the beam axis), in order to break the conditions leading to degeneracy.

7. Azimuthal index detection with low photon counts

To test the performances of the interferometer in detecting LG beam states with high sensitivity, we push the system into the regime of low photon counts. To this aim, a small portion of the interference pattern is selected through a narrow slit with aperture 50 μm, much smaller than the fringe period. The slit is oriented parallel to the interference fringes along the y direction. The light transmitted by the slit is focused by a positive lens into a single-mode fiber. The extremely small aperture of the fiber (roughly 8 μm) and the tight alignment requirements for proper lens-fiber coupling ensure that only few photons are collected. The resulting photon counts are read by a photomultiplier and converted to electric pulses measured by a fast acquisition card (Picoscope 4224 A).

We adjust the lateral position of the slit across the interference plane (the x coordinate in Eq. (4)) to properly set the working point of the detector close to the region of the interference pattern with the highest intensity derivative, to maximize sensibility [53]. Notice that this is made possible by the small, albeit finite wavefront curvature imposed by the positive lens before the interferometer, which results in interference fringes with a finite periodicity. Contrarily, for a perfectly collimated LG beam with vanishing curvature, a uniform intensity pattern would form downstream the crystal, as previously discussed. Therefore, based on Eq. (4), we optimize the states separation by experimentally setting the working point of the interferometer to $k_f x + \phi_0 \approx \pi(m + 1/2)$, where m is an integer [53]. We do so by sending an $l = 0$ state (corresponding to a standard Gaussian beam) to the interferometer, and by adjusting the slit position halfway between the maximum and the minimum intensity of an interference fringe [53].

After this initial calibration, counts relative to the different LG beam states $l = -1$, $l = 1$, $l = -2$, $l = 2$ have been measured, each in an interval time of 100 ms, with the selection slit fixed at the specified position x. Since the overall LG beam intensity depends on the value of the azimuthal index, as evident from Eq. (2), for each value of the azimuthal index counts are then normalized to their maximum value, which is obtained by scanning the position of the selection slit to find the closest maximum in the fringe pattern. With reference to Eq. (4), the absolute counts at the specific point x would correspond to $I(x)$, and the maximum counts in correspondence of the interference maximum to $4I_0$. Thus, the normalized counts $I(x)/4I_0$ provide a measurement of the argument of the interference term in Eq. (4). Then the reference value from the TEM_{00} mode is used to isolate to linear term $l\Delta\theta$, hence the value of the azimuthal index can be inferred. This enables direct comparison among the different LG beam states, regardless of the overall intensity level I_0 in Eq. (4) for the different LG beams. Notice that this is similar to the normalization procedure adopted in Eq. (5). Results are shown in Fig. 6 and are summarized in Table 1. The four LG beam states are well distinguishable by using less than 160 photon counts only. Notice that the splitting of the states $l = \pm 2$ is twice as much that of the states $l = \pm 1$, as predicted by theory.

Finally, to quantify the stability of the interferometer, we monitored any eventual drift of the interference fringes generated by either the $l = -1$ or the $l = -4$ LG beam over long acquisitions. In the worst case, we measured a maximum phase change of less than 0.25 rad over more than one hour, corresponding to a phase drift of 70 μrad/s, likely in presence of mechanical or thermal relaxations. The impact on our measurements is definitely negligible, since this maximum drift would introduce a phase shift 30 times smaller than the measured phase change of 0.513 rad between the two images acquired with a temporal delay of 240 s in Fig. 5, and orders of magnitude smaller than the phase changes between either the $l = \pm 1$ states or the $l = \pm 2$ states during experiments with low photon counts, with acquisitions being performed over a total time of 200 ms. This proves that the monolithic interferometer fulfills the requirements of stability during normal operations, and does not require any thermal drift compensation to distinguish different LG beam states over minutes-long acquisitions.

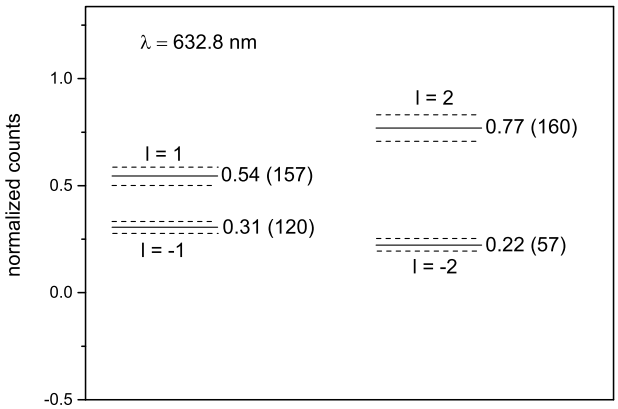

Fig. 6. Normalized counts obtained with the monolithic interferometer working in the regime of weak LG beams. Dashed lines show the statistical errors. Absolute photon counts are shown in brackets.

8. Conclusions

In this work we have shown high sensitive strictly-local identification of azimuthal index of LG beams with less than 160 photon counts. To this aim, we have designed and demonstrated an intrinsically stable monolithic interferometer based on a birefringent calcite crystal, which does not require any feedback or thermal drift compensation. By first generating a reference interference pattern with a standard TEM_{00} mode, we then detect the value of the azimuthal index of a LG beam from the lateral shift of the pattern with respect to the reference one. Such differential analysis allows to automatically account for spurious phase contributions, such as common tilts, on top of the helical wavefront of the LG beam. Remarkably, the method exploits only a very small portion of the entire wavefront ($f = 5\%$ in our case), thus improving over previous techniques. An experimental setup has been realized to prove the effectiveness of the proposed scheme through the absolute measurement of the phase shifts induced by changes of the azimuthal index. Experimental results are in good agreement with theory. Furthermore, the high stability of the interferometer allows collecting sufficient statistics to measure the azimuthal index of very weak LG beams with few photon counts. Results with values of the azimuthal index $l = -1$, $l = 1$, $l = -2$ and $l = 2$ prove, for the first time to our knowledge, that LG beam states can be detected with only a few hundreds of photon counts in a strictly local manner, opening new perspectives for high sensitive local measurements of LG beam radiation not requiring thermal drifts compensation and with high resilience to mechanical vibrations.

In our current setup, experiments with weak LG beams have been conducted by operating the monolithic interferometer in combination with a single slit, a positive lens and a single-mode fiber. Therefore, the sensibility can be further increased by employing e.g. a periodic array of slits, or a grating, having the same fringe periodicity. Acting

on several fringes simultaneously, the overall accuracy and sensibility can then be greatly enhanced. This is not necessary when the wavefront curvature approaches zero, since the light intensity eventually concentrates in a single fringe (with infinite periodicity) downstream the crystal. Furthermore, the normalization procedure adopted here involves collecting the absolute photon counts and the maximum photon counts in the interference pattern with two subsequent measurements. While this is certainly valid for this proof-of-principle experiment, in a real scenario it might be more adequate to implement additional devices. For example, by using a beam splitter in between the birefringent crystal and the polarizer, it should be possible to achieve simultaneous measurements of the absolute counts on the arm equipped with the polarizer, for which interference occurs, and of the total counts on the other one.

The proposed method can be advantageously applied to high sensitive detection of LG beam states down to the photon counting regime, even when it is not possible to access the entire wavefront of the radiation beam or the position of the beam axis cannot be precisely aligned. Our findings are likely to foster the development of new detection schemes in the quantum regime, and pave the way to effective characterization of LG beam states in quantum technology. In the future, it may also be of interest to test the method with vector-vortex beams, a class of OAM radiation states which also exhibit a spatially-dependent polarization pattern.

CRediT authorship contribution statement

Mirko Siano: Writing – review & editing, Writing – original draft, Visualization, Validation, Software, Methodology, Formal analysis, Data curation, Conceptualization. **Bruno Paroli:** Writing – review & editing, Writing – original draft, Visualization, Validation, Software, Methodology, Formal analysis, Data curation, Conceptualization. **Simone Cialdi:** Writing – review & editing, Writing – original draft, Methodology, Formal analysis, Conceptualization. **Stefano Olivares:** Writing – review & editing, Writing – original draft, Methodology. **Matteo G.A. Paris:** Writing – review & editing, Writing – original draft, Methodology. **Edoardo Suerra:** Writing – review & editing, Writing – original draft, Methodology. **Marco A.C. Potenza:** Writing – review & editing, Writing – original draft, Validation, Methodology, Formal analysis, Conceptualization.

Declaration of competing interest

The authors declare that they have no known competing financial interests or personal relationships that could have appeared to influence the work reported in this paper.

Data availability

Data will be made available on request.

Acknowledgments

This work was supported by the National Institute for Nuclear Physics (INFN) (project: ADAMANT).

References

[1] L. Allen, M.W. Beijersbergen, R.J.C. Spreeuw, J.P. Woerdman, Orbital angular momentum of light and the transformation of Laguerre-Gaussian laser modes, Phys. Rev. A 45 (1992) 8185–8189, http://dx.doi.org/10.1103/PhysRevA.45.8185, URL https://link.aps.org/doi/10.1103/PhysRevA.45.8185.

[2] M. Soskin, S.V. Boriskina, Y. Chong, M.R. Dennis, A. Desyatnikov, Singular optics and topological photonics, J. Opt. 19 (1) (2016) 010401, http://dx.doi.org/10.1088/2040-8986/19/1/010401.

[3] A. Mair, A. Vaziri, G. Weihs, A. Zeilinger, Entanglement of the orbital angular momentum states of photons, Nature 412 (6844) (2001) 313–316, http://dx.doi.org/10.1038/35085529.

[4] Y. Ma, G. Rui, B. Gu, Y. Cui, Trapping and manipulation of nanoparticles using multifocal optical vortex metalens, Sci. Rep. 7 (2017) 14611, http://dx.doi.org/10.1038/s41598-017-14449-y.

[5] F. Tamburini, G. Anzolin, G. Umbriaco, A. Bianchini, C. Barbieri, Overcoming the Rayleigh criterion limit with optical vortices, Phys. Rev. Lett. 97 (2006) 163903, http://dx.doi.org/10.1103/PhysRevLett.97.163903, URL https://link.aps.org/doi/10.1103/PhysRevLett.97.163903.

[6] G. Anzolin, F. Tamburini, A. Bianchini, G. Umbriaco, C. Barbieri, Optical vortices with starlight, Astron. Astrophys. 488 (3) (2008) 1159–1165, http://dx.doi.org/10.1051/0004-6361:200810469.

[7] F. Tamburini, B. Thidé, G. Molina-Terriza, G. Anzolin, Twisting of light around rotating black holes, Nat. Phys. 7 (2011) 195–197, http://dx.doi.org/10.1038/nphys1907.

[8] G.A. Swartzlander, E.L. Ford, R.S. Abdul-Malik, L.M. Close, M.A. Peters, D.M. Palacios, D.W. Wilson, Astronomical demonstration of an optical vortex coronagraph, Opt. Express 16 (14) (2008) 10200–10207, http://dx.doi.org/10.1364/OE.16.010200, URL https://opg.optica.org/oe/abstract.cfm?URI=oe-16-14-10200.

[9] D. Mawet, E. Serabyn, K. Liewer, R. Burruss, J. Hickey, D. Shemo, The vector vortex coronagraph: laboratory results and first light at palomar observatory, Astrophys. J. 709 (1) (2009) 53, http://dx.doi.org/10.1088/0004-637X/709/1/53.

[10] E. Serabyn, C.M. Prada, P. Chen, D. Mawet, Vector vortex coronagraphy for exoplanet detection with spatially variant diffractive waveplates, J. Opt. Soc. Amer. B 36 (5) (2019) D13–D19, http://dx.doi.org/10.1364/JOSAB.36.000D13, URL https://opg.optica.org/josab/abstract.cfm?URI=josab-36-5-D13.

[11] A. Picón, J. Mompart, J.R.V. de Aldana, L. Plaja, G.F. Calvo, L. Roso, Photoionization with orbital angular momentum beams, Opt. Express 18 (4) (2010) 3660–3671, http://dx.doi.org/10.1364/OE.18.003660, URL https://opg.optica.org/oe/abstract.cfm?URI=oe-18-4-3660.

[12] C.T. Schmiegelow, J. Schulz, H. Kaufmann, T. Ruster, U.G. Poschinger, F. Schmidt-Kaler, Transfer of optical orbital angular momentum to a bound electron, Nature Commun. 7 (1) (2016) 12998, http://dx.doi.org/10.1038/ncomms12998.

[13] F. Tamburini, E. Mari, A. Sponselli, B. Thidé, A. Bianchini, F. Romanato, Encoding many channels on the same frequency through radio vorticity: first experimental test, New J. Phys. 14 (3) (2012) 033001, http://dx.doi.org/10.1088/1367-2630/14/3/033001.

[14] Y. Yan, G. Xie, M.P.J. Lavery, H. Huang, N. Ahmed, C. Bao, Y. Ren, Y. Cao, L. Li, Z. Zhao, A.F. Molisch, M. Tur, M.J. Padgett, A.E. Willner, High-capacity millimetre-wave communications with orbital angular momentum multiplexing, Nature Commun. 5 (2014) 4876, http://dx.doi.org/10.1038/ncomms5876.

[15] M. Krenn, R. Fickler, M. Fink, J. Handsteiner, M. Malik, T. Scheidl, R. Ursin, A. Zeilinger, Communication with spatially modulated light through turbulent air across vienna, New J. Phys. 16 (11) (2014) 113028, http://dx.doi.org/10.1088/1367-2630/16/11/113028.

[16] G. Xie, Y. Ren, Y. Yan, H. Huang, N. Ahmed, L. Li, Z. Zhao, C. Bao, M. Tur, S. Ashrafi, A.E. Willner, Experimental demonstration of a 200-Gbit/s free-space optical link by multiplexing Laguerre–Gaussian beams with different radial indices, Opt. Lett. 41 (15) (2016) 3447–3450, http://dx.doi.org/10.1364/OL.41.003447, URL https://opg.optica.org/ol/abstract.cfm?URI=ol-41-15-3447.

[17] J. Tan, Z. Zhao, Y. Wang, Z. Zhang, J. Liu, N. Zhu, 12.5 Gb/s multi-channel broadcasting transmission for free-space optical communication based on the optical frequency comb module, Opt. Express 26 (2) (2018) 2099–2106, http://dx.doi.org/10.1364/OE.26.002099, URL https://opg.optica.org/oe/abstract.cfm?URI=oe-26-2-2099.

[18] W.-C. Wang, H.-Y. Wang, G.-R. Lin, Ultrahigh-speed violet laser diode based free-space optical communication beyond 25 Gbit/s, Sci. Rep. 8 (2018) 13142, http://dx.doi.org/10.1038/s41598-018-31431-4.

[19] N. Bozinovic, Y. Yue, Y. Ren, M. Tur, P. Kristensen, H. Huang, A.E. Willner, S. Ramachandran, Terabit-scale orbital angular momentum mode division multiplexing in fibers, Science 340 (6140) (2013) 1545–1548, http://dx.doi.org/10.1126/science.1237861, arXiv:https://www.science.org/doi/pdf/10.1126/science.1237861.

[20] L. Zhu, A. Wang, S. Chen, J. Liu, J. Wang, Orbital angular momentum mode multiplexed transmission in heterogeneous few-mode and multi-mode fiber network, Opt. Lett. 43 (8) (2018) 1894–1897, http://dx.doi.org/10.1364/OL.43.001894, URL https://opg.optica.org/ol/abstract.cfm?URI=ol-43-8-1894.

[21] Z. Wang, N. Zhang, X.-C. Yuan, High-volume optical vortex multiplexing and demultiplexing for free-space optical communication, Opt. Express 19 (2) (2011) 482–492, http://dx.doi.org/10.1364/OE.19.000482, URL https://opg.optica.org/oe/abstract.cfm?URI=oe-19-2-482.

[22] J. Wang, J.-Y. Yang, I.M. Fazal, N. Ahmed, Y. Yan, H. Huang, Y. Ren, Y. Yue, S. Dolinar, M. Tur, A.E. Willner, Terabit free-space data transmission employing orbital angular momentum multiplexing, Nature Photon. 6 (2012) 488–496, http://dx.doi.org/10.1038/nphoton.2012.138.

[23] B. Guan, R.P. Scott, C. Qin, N.K. Fontaine, T. Su, C. Ferrari, M. Cappuzzo, F. Klemens, B. Keller, M. Earnshaw, S.J.B. Yoo, Free-space coherent optical communication with orbital angular, momentum multiplexing/demultiplexing using a hybrid 3D photonic integrated circuit, Opt. Express 22 (1) (2014) 145–156, http://dx.doi.org/10.1364/OE.22.000145, URL https://opg.optica.org/oe/abstract.cfm?URI=oe-22-1-145.

[24] L. Li, R. Zhang, Z. Zhao, G. Xie, P. Liao, K. Pang, H. Song, C. Liu, Y. Ren, G. Labroille, P. Jian, D. Starodubov, B. Lynn, R. Bock, M. Tur, A.E. Willner, High-capacity free-space optical communications between a ground transmitter and a ground receiver via a UAV using multiplexing of multiple orbital-angular-momentum beams, Sci. Rep. 7 (2017) 17427, http://dx.doi.org/10.1038/s41598-017-17580-y.

[25] J. Vickers, M. Burch, R. Vyas, S. Singh, Phase and interference properties of optical vortex beams, J. Opt. Soc. Amer. A 25 (3) (2008) 823–827, http://dx.doi.org/10.1364/JOSAA.25.000823, URL https://opg.optica.org/josaa/abstract.cfm?URI=josaa-25-3-823.

[26] Y. Shen, G.T. Campbell, B. Hage, H. Zou, B.C. Buchler, P.K. Lam, Generation and interferometric analysis of high charge optical vortices, J. Opt. 15 (4) (2013) 044005, http://dx.doi.org/10.1088/2040-8978/15/4/044005.

[27] H. Zhou, S. Yan, J. Dong, X. Zhang, Double metal subwavelength slit arrays interference to measure the orbital angular momentum and the polarization of light, Opt. Lett. 39 (11) (2014) 3173–3176, http://dx.doi.org/10.1364/OL.39.003173, URL https://opg.optica.org/ol/abstract.cfm?URI=ol-39-11-3173.

[28] G. Ruffato, M. Massari, G. Parisi, F. Romanato, Test of mode-division multiplexing and demultiplexing in free-space with diffractive transformation optics, Opt. Express 25 (7) (2017) 7859–7868, http://dx.doi.org/10.1364/OE.25.007859, URL https://opg.optica.org/oe/abstract.cfm?URI=oe-25-7-7859.

[29] M.P.J. Lavery, D.J. Robertson, G.C.G. Berkhout, G.D. Love, M.J. Padgett, J. Courtial, Refractive elements for the measurement of the orbital angular momentum of a single photon, Opt. Express 20 (3) (2012) 2110–2115, http://dx.doi.org/10.1364/OE.20.002110, URL https://opg.optica.org/oe/abstract.cfm?URI=oe-20-3-2110.

[30] C. Li, S. Zhao, Efficient separating orbital angular momentum mode with radial varying phase, Photon. Res. 5 (4) (2017) 267–270, http://dx.doi.org/10.1364/PRJ.5.000267, URL https://opg.optica.org/prj/abstract.cfm?URI=prj-5-4-267.

[31] G.C.G. Berkhout, M.P.J. Lavery, J. Courtial, M.W. Beijersbergen, M.J. Padgett, Efficient sorting of orbital angular momentum states of light, Phys. Rev. Lett. 105 (2010) 153601, http://dx.doi.org/10.1103/PhysRevLett.105.153601, URL https://link.aps.org/doi/10.1103/PhysRevLett.105.153601.

[32] M. Mirhosseini, M. Malik, Z. Shi, R.W. Boyd, Efficient separation of the orbital angular momentum eigenstates of light, Nature Commun. 4 (2013) 2781, http://dx.doi.org/10.1038/ncomms3781.

[33] G. Kulkarni, R. Sahu, O.S. Magaña-Loaiza, R.W. Boyd, A.K. Jha, Single-shot measurement of the orbital-angular-momentum spectrum of light, Nature Commun. 8 (2017) 1054, http://dx.doi.org/10.1038/s41467-017-01215-x.

[34] A.E. Willner, H. Huang, Y. Yan, Y. Ren, N. Ahmed, G. Xie, C. Bao, L. Li, Y. Cao, Z. Zhao, J. Wang, M.P.J. Lavery, M. Tur, S. Ramachandran, A.F. Molisch, N. Ashrafi, S. Ashrafi, Optical communications using orbital angular momentum beams, Adv. Opt. Photon. 7 (1) (2015) 66–106, http://dx.doi.org/10.1364/AOP.7.000066, URL https://opg.optica.org/aop/abstract.cfm?URI=aop-7-1-66.

[35] J. Leach, J. Courtial, K. Skeldon, S.M. Barnett, S. Franke-Arnold, M.J. Padgett, Interferometric methods to measure orbital and spin, or the total angular momentum of a single photon, Phys. Rev. Lett. 92 (2004) 013601, http://dx.doi.org/10.1103/PhysRevLett.92.013601, URL https://link.aps.org/doi/10.1103/PhysRevLett.92.013601.

[36] T. Lei, M. Zhang, Y. Li, P. Jia, G.N. Liu, X. Xu, Z. Li, C. Min, J. Lin, C. Yu, H. Niu, X. Yuan, Massive individual orbital angular momentum channels for multiplexing enabled by dammann gratings, Light Sci. Appl. 4 (2015) e257, http://dx.doi.org/10.1038/lsa.2015.30.

[37] T. Doster, A.T. Watnik, Machine learning approach to OAM beam demultiplexing via convolutional neural networks, Appl. Opt. 56 (12) (2017) 3386–3396, http://dx.doi.org/10.1364/AO.56.003386, URL https://opg.optica.org/ao/abstract.cfm?URI=ao-56-12-3386.

[38] V. Raskatla, B.P. Singh, S. Patil, V. Kumar, R.P. Singh, Speckle-based deep learning approach for classification of orbital angular momentum modes, J. Opt. Soc. Amer. A 39 (4) (2022) 759–765, http://dx.doi.org/10.1364/JOSAA.446352, URL https://opg.optica.org/josaa/abstract.cfm?URI=josaa-39-4-759.

[39] S. Avramov-Zamurovic, J.M. Esposito, C. Nelson, Classifying beams carrying orbital angular momentum with machine learning: Tutorial, J. Opt. Soc. Amer. A 40 (1) (2023) 64–77, http://dx.doi.org/10.1364/JOSAA.474611, URL https://opg.optica.org/josaa/abstract.cfm?URI=josaa-40-1-64.

[40] S. Avramov-Zamurovic, A.T. Watnik, J.R. Lindle, K.P. Judd, J.M. Esposito, Machine learning-aided classification of beams carrying orbital angular momentum propagated in highly turbid water, J. Opt. Soc. Amer. A 37 (10) (2020) 1662–1672, http://dx.doi.org/10.1364/JOSAA.401153, URL https://opg.optica.org/josaa/abstract.cfm?URI=josaa-37-10-1662.

[41] P.L. Neary, J.M. Nichols, A.T. Watnik, K.P. Judd, G.K. Rohde, J.R. Lindle, N.S. Flann, Transport-based pattern recognition versus deep neural networks in underwater OAM communications, J. Opt. Soc. Amer. A 38 (7) (2021) 954–962, http://dx.doi.org/10.1364/JOSAA.412463, URL https://opg.optica.org/josaa/abstract.cfm?URI=josaa-38-7-954.

[42] Z. Wang, M. Chen, M. Wan, J. Ren, J. Ding, Coherent demodulated underwater wireless optical communication system based on convolutional neural network, Opt. Commun. 534 (2023) 129316, http://dx.doi.org/10.1016/j.optcom.2023.129316, URL https://www.sciencedirect.com/science/article/pii/S0030401823000615.

[43] H. Zhan, L. Wang, W. Wang, S. Zhao, Hybrid opto-electronic deep neural network based orbital angular momentum mode recognition scheme in oceanic turbulence, J. Opt. Soc. Amer. B 40 (1) (2023) 187–193, http://dx.doi.org/10.1364/JOSAB.474443, URL https://opg.optica.org/josab/abstract.cfm?URI=josab-40-1-187.

[44] A.E. Willner, K. Pang, H. Song, K. Zou, H. Zhou, Orbital angular momentum of light for communications, Appl. Phys. Rev. 8 (4) (2021) 041312, http://dx.doi.org/10.1063/5.0054885.

[45] D.M. Fatkhiev, M.A. Butt, E.P. Grakhova, R.V. Kutluyarov, I.V. Stepanov, N.L. Kazanskiy, S.N. Khonina, V.S. Lyubopytov, A.K. Sultanov, Recent advances in generation and detection of orbital angular momentum optical beams—A review, Sensors 21 (15) (2021) http://dx.doi.org/10.3390/s21154988, URL https://www.mdpi.com/1424-8220/21/15/4988.

[46] J. Wang, J. Liu, S. Li, Y. Zhao, J. Du, L. Zhu, Orbital angular momentum and beyond in free-space optical communications, Nanophotonics 11 (4) (2022) 645–680, http://dx.doi.org/10.1515/nanoph-2021-0527.

[47] B. Chen, Y. Wei, T. Zhao, S. Liu, R. Su, B. Yao, Y. Yu, J. Liu, X. Wang, Bright solid-state sources for single photons with orbital angular momentum, Nat. Nanotechnol. 16 (2021) 302–307, http://dx.doi.org/10.1038/s41565-020-00827-7.

[48] C. Wu, S. Kumar, Y. Kan, D. Komisar, Z. Wang, S.I. Bozhevolnyi, F. Ding, Room-temperature on-chip orbital angular momentum single-photon sources, Sci. Adv. 8 (2) (2022) eabk3075, http://dx.doi.org/10.1126/sciadv.abk3075, arXiv:https://www.science.org/doi/pdf/10.1126/sciadv.abk3075.

[49] V. Kumar, V. Sharma, S. Singh, S.C. Kumar, A. Forbes, M. Ebrahim-Zadeh, G.K. Samanta, Imaging inspired characterization of single photons carrying orbital angular momentum, AVS Quantum Sci. 4 (1) (2022) 015001, http://dx.doi.org/10.1116/5.0078870.

[50] B. Paroli, M. Siano, M.A.C. Potenza, Measuring the topological charge of orbital angular momentum radiation in single-shot by means of the wavefront intrinsic curvature, Appl. Opt. 59 (17) (2020) 5258–5264, http://dx.doi.org/10.1364/AO.392341, URL https://opg.optica.org/ao/abstract.cfm?URI=ao-59-17-5258.

[51] B. Paroli, M. Siano, M. Potenza, A composite beam of radiation with orbital angular momentum allows effective local, single-shot measurement of topological charge, Opt. Commun. 459 (2020) 125049, http://dx.doi.org/10.1016/j.optcom.2019.125049, URL https://www.sciencedirect.com/science/article/pii/S0030401819310892.

[52] B. Paroli, M. Siano, M.A.C. Potenza, Dense-code free space transmission by local demultiplexing optical states of a composed vortex, Opt. Express 29 (10) (2021) 14412–14424, http://dx.doi.org/10.1364/OE.417772, URL https://opg.optica.org/oe/abstract.cfm?URI=oe-29-10-14412.

[53] B. Paroli, L. Cremonesi, M. Siano, M. Potenza, Hybrid OAM-amplitude multiplexing and demultiplexing of incoherent optical states, Opt. Commun. 524 (2022) 128808, http://dx.doi.org/10.1016/j.optcom.2022.128808, URL https://www.sciencedirect.com/science/article/pii/S0030401822005168.

[54] J.W. Goodman, Statistical Optics, John Wiley & Sons, Inc, New York, 2000.